

Selection of Actuation Mode for Tensegrity Mechanisms: the Case Study of the Actuated Snelson Cross

Jeremy Begey^{a,b,*}, Marc Vedrines^a, Nicolas Andreff^b, Pierre Renaud^a

^a*ICube - University of Strasbourg - INSA Strasbourg*

^b*Femto-ST - University of Franche-Comté - ENSMM*

Abstract

Tensegrity mechanisms are self-stressed and deployable mechanisms which provide interesting properties such as high resistance-to-mass ratio and compliance. Despite a growing interest for these mechanisms in robotics, the actuation selection of such mechanisms is still poorly discussed. In this paper, the influence of the actuation type and position, *i.e.* actuation mode, within the structure is assessed for a widely considered tensegrity mechanism, the Snelson cross. Actuation strategies of interest are proposed and performance criteria are defined to achieve fair comparison of the mechanisms. Performance maps are generated and the most interesting results are discussed. Finally, building blocks providing elementary motions are identified and compliant equivalences of conventional joints are proposed for the design of more complex tensegrity-based devices.

Keywords: Tensegrity mechanisms, Deployable structures, Mechanism evaluation, Actuation selection, Mechanism design

1. Introduction

Tensegrities are self-stressed mechanical structures composed of bodies in compression, called bars or struts, linked together with a network of tensile elements, *e.g.* cables [33], providing a high resistance-to-mass ratio [32]. These last twenty years, authors focused on designing actuated tensegrities, called Tensegrity Mechanisms (TM¹), in which elastic elements are used, *e.g.* springs [2], so they are compliant. In addition to having a high resistance for a lightweight structure, TM provide

*Corresponding author: jeremy.begey@etu.unistra.fr, 24 rue Alain Savary 25000 Besançon, France

¹Appendix A contains a list of acronyms and symbols used through the article.

interesting properties for contact management thanks to the self-stress property allowing adaptable stiffness [11, 5]. Their deployability also allows a large workspace for compact structures [36], making them of high interest for robot design. Therefore, TM are considered in many robotic devices such as mobile robots [29, 19, 14], manipulators [4, 1], bio-inspired devices [22], variable stiffness mechanisms [5], robot graspers [34] or medical devices [7].

Multiple types of actuation have been considered for TM. Modulation of the length of tensile elements has been proposed using winding of non-elastic cables [4], non-elastic cables placed in series with springs [14], elastic cables [27] or also by actuating pneumatic muscles [17] or Shape Memory Alloys (SMA) [30]. Linear actuation of bars was also proposed by using piezo-electric actuators [5], prismatic actuators [1] and SMA [25]. Other actuation types have also been proposed for the actuation of cable- or spring-based devices, such as stiffness modulation [39], that can be of interest to TM as well. A large choice of actuation solutions is then available for this kind of mechanism if we consider freedom in the selection of actuation type, position and number of actuators. In the following, we define an actuation mode as a set of one actuation type, a number of actuators and the position of these actuators within the TM.

In [23], an optimization method was used to determine the number and the position of the actuators for a given TM. However, a single type of actuator was considered and the TM architecture was selected before the use of the method. The selection process of the actuation mode of a TM during the design is thus poorly discussed. Therefore, we propose to carry out a thorough study of the impact of the actuation mode on the behavior of a TM.

The Snelson Cross (SC) [33] is a planar tensegrity composed of two bars linked to each other with four cables forming a cross-shaped structure. It has been interestingly used to design multiple TM for soft mobile robots [21], bio-mimetic applications [15] or energy harvesting devices [37] to name a few. Moreover, several actuation modes of this TM were considered [4, 10, 38, 15, 21]. At the same time, its reduced number of constructive elements allows to perform a thorough analysis of the actuation modes. The SC is then considered as the tensegrity of interest for this case study.

TM are self-stressed mechanisms. As a consequence, geometric and kinematic criteria are not sufficient to assess them. The evaluation of internal forces is in particular very important. Therefore, we discuss in this paper performance criteria to evaluate TM behavior and introduce specific ones. They are used to assess the impact of actuation modes on a SC, which constitutes the first contribution. The SC was used in the literature to build more complex TM by assembly [27, 15, 3, 18]. Motivated by the design of modular passive structures [8], and as a second

contribution, results of our study are used to determine building blocks of interest for TM design.

Section 2 of this paper exposes the focus of the SC study and the considered actuation modes. In Section 3, the models of the selected actuated SC are derived and the way to compute a tensegrity configuration is presented. Section 4 describes the proposed performance criteria used to assess a TM. Results from the study are displayed and analyzed in Section 5. Section 6 then discusses the proposed building blocks and their properties. Finally, conclusions are drawn and perspectives are proposed in Section 7.

2. Actuation modes of SC

2.1. Description of the reference SC

In the following, TM are built by introducing actuators in a so-called reference SC. This structure is passive and compliant. It is composed, as represented in Fig. 1, of two rigid bars of length L_{13} and L_{24} , linking respectively nodes A_1 and A_3 and nodes A_2 and A_4 . Linear springs are generally considered as tensile elements in TM [29, 14, 4, 9]. For sake of analysis simplicity, these springs have been considered with zero free-length [2, 38]. However, in practical implementations, springs with zero free-length are difficult to integrate [31]. Linear springs with non-zero free length are then selected as elastic elements. For sake of representation simplicity, a symmetrical architecture with respect to the y axis is considered with prismatic joints at nodes A_1 and A_4 and an attachment point at the origin of the base frame (Fig.1). Because of these mounting conditions, two springs are located at the base. To simplify notations, each side of the SC is then composed of two serially connected springs, whose assembly creates an elastic element of stiffness K and free-length l_0 . Each spring possesses a stiffness $2K$ and a free-length $l_0/2$. A platform of centroid \mathbf{g} is connected to nodes A_2 and A_3 as illustrated in Fig. 1. In the remainder of the paper, gravity is not considered and all joints are assumed to be frictionless.

2.2. Types of actuation

Tensegrity Mechanisms (TM) are obtained from the reference Snelson Cross (SC) by adding actuation elements. We consider that these elements are of same type, *i.e.* we do not mix for instance bar actuation and cable actuation. This will help us to understand the impact of each actuation type.

First, it is possible to vary the length of the bars which are initially rigid. The resulting TM is designated as a bar-actuated (BA) SC. Second, the free-length or the stiffness of the springs can be modulated. The TM we obtain using these two

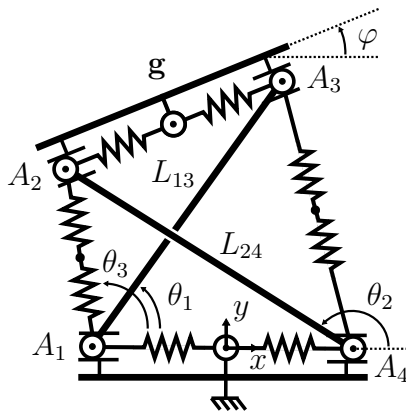


Figure 1: Reference SC used to build the TMs.

types of actuation are designated respectively as Free-length-Actuated (FA) SC and Stiffness-Actuated (SA) SC. Third, it is also possible to directly control the length of the tensile elements. This can be achieved by replacing some springs by non-elastic cables whose lengths are controlled. We designate accordingly the TM in such a case as a Cable-Actuated (CA) SC. As a summary, four actuation types are considered and corresponding TM are labelled in the following as BA, FA, SA and CA.

2.3. Number and position of actuators

A SC is compliant if at least one unconstrained Degree of Freedom (DoF) exists in the mechanism. It was shown in [2] that a minimal number of two springs must then be used in a compliant SC. In the case of CA, it implies that a maximum of two cables can replace springs. This number of actuators is considered for all TM in the following in order to obtain as many mobilities as possible and at the same time to achieve a fair comparison of the proposed actuation types.

For BA, only one location of the actuators is possible as the SC only has two bars that thus become actuated. Since the SC contains four tensile elements, six different sets of positions for two actuators controlling tensile elements are possible. Taking into account the mechanism symmetry, the analysis can be conducted considering only four sets of actuator positions, which are represented in Table 1 and denoted M_i , $i \in [1, 4]$.

With three different actuation types (FA, SA, CA) to control the tensile elements, it leads to twelve actuation modes. Finally, adding the actuation of BA, a total of thirteen different actuation modes are considered. Each one of them is named and listed in Table 1.

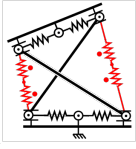
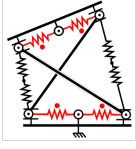
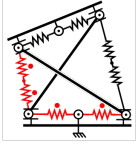
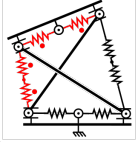
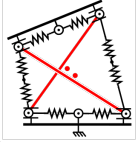
Actuator positions		Actuation types			
Designation	Representation	Free-length-actuated (FA)	Stiffness-actuated (SA)	Cable-actuated (CA)	Bar-actuated (BA)
M_1		FA1	SA1	CA1	
M_2		FA2	SA2	CA2	
M_3		FA3	SA3	CA3	
M_4		FA4	SA4	CA4	
L_{13} and L_{24}					BA

Table 1: The thirteen actuation modes with respect to the actuator positions and types. The actuated SC are displayed with the actuated elements drawn in red and designated with a point next to their representation (for CA, they are replaced by non-elastic cables).

3. Modeling

3.1. Tensegrity configuration

The platform of centroid \mathbf{g} (Fig. 1) is the end-effector and its pose is noted \mathbf{x} . The TM being planar, $\mathbf{x} = [\mathbf{g}^T, \varphi]^T$ with φ the orientation of the platform with respect

to the base. The pose \mathbf{x} can be expressed using the node coordinates

$$\mathbf{g} = \frac{A_2 + A_3}{2} \quad \varphi = \arctan \left(\frac{\overrightarrow{A_2 A_3^T \vec{y}}}{\overrightarrow{A_2 A_3^T \vec{x}}} \right) \quad (1)$$

Thereby, the pose can be directly estimated from the node coordinates.

We denote \mathbf{q} the vector of the actuated variables, designated as the joint coordinates. TM are compliant so there exists some unconstrained coordinates that we denote \mathbf{q}_u . The choice of these coordinates depends on the position of the actuators. It will be highlighted in the following. A TM can then be fully described by the vector of generalized coordinates $\mathbf{q}_g = [\mathbf{q}^T, \mathbf{q}_u^T]^T$. A tensegrity configuration is obtained when \mathbf{q}_g is solution of the following equations and conditions [9]

$$\begin{cases} \Phi(\mathbf{q}_g) = \mathbf{0} \\ \frac{\partial U(\mathbf{q}_g)}{\partial \mathbf{q}_u} = \mathbf{0} \\ \frac{\partial^2 U(\mathbf{q}_g)}{\partial \mathbf{q}_u^2} > \mathbf{0} \\ \mathbf{t}_t(\mathbf{q}_g) > \mathbf{0} \end{cases} \quad (2)$$

which expresses that the geometrical loop closure equations $\Phi(\mathbf{q}_g)$ are verified, all tensions in the tensile elements $\mathbf{t}_t(\mathbf{q}_g)$ are positive, and a stable equilibrium is obtained. Equilibrium existence and stability are defined using the first and second derivatives of the potential energy $U(\mathbf{q}_g)$.

Modeling then consists in deriving the node coordinates and the potential energy. It is performed for the TM associated to the thirteen actuation modes in two phases. The first one is dedicated to the modeling of BA, FA and SA, and the second one to the modeling of CA.

3.2. Modeling of BA, FA and SA

When BA, FA or SA are considered, the TM includes four springs (Fig. 1). The SC then presents three unconstrained DoF according to [2, 6], implying that $\mathbf{q}_u \in \mathbb{R}^3$. The angles θ_1 , θ_2 and θ_3 define the orientations of the two bars and one spring as displayed in Fig. 1. Therefore $\mathbf{q}_u = [\theta_1, \theta_2, \theta_3]^T$. Using geometrical considerations in triangles $A_i A_j A_k$, $\{i, j, k\} \in [1, 2, 3, 4]$, $i \neq j \neq k$ and the loop closure equations

Mode	\mathbf{q}	Mode	\mathbf{q}	Mode	\mathbf{q}	Mode	\mathbf{q}
FA1	$[l_{012}, l_{034}]^T$	FA2	$[l_{014}, l_{023}]^T$	FA3	$[l_{014}, l_{012}]^T$	FA4	$[l_{012}, l_{023}]^T$
SA1	$[K_{12}, K_{34}]^T$	SA2	$[K_{14}, K_{23}]^T$	SA3	$[K_{14}, K_{12}]^T$	SA4	$[K_{12}, K_{23}]^T$
BA	$[L_{13}, L_{24}]^T$						

Table 2: Joint coordinates \mathbf{q} of each TM, defined in Tab. 1.

$\Phi(\mathbf{q}_{\mathbf{g}})$, the nodes coordinates can be written as

$$\begin{aligned}
A_1 &= \begin{bmatrix} -\frac{L_{14}}{2} & 0 \end{bmatrix}^T & A_4 &= -A_1 \\
A_2 &= A_1 + L_{12} [\cos(\theta_3) \quad \sin(\theta_3)]^T \\
A_3 &= A_1 + L_{13} [\cos(\theta_1) \quad \sin(\theta_1)]^T
\end{aligned} \tag{3}$$

with

$$\begin{aligned}
L_{12} &= L_{24} \frac{\sin(\theta_2)}{\sin(\theta_3)} \\
L_{14} &= L_{12} \cos(\theta_3) - L_{24} \cos(\theta_2)
\end{aligned} \tag{4}$$

In (3) and (4), L_{ij} is the distance between nodes A_i and A_j . Assembly limits are defined by $\theta_i \in [0, \pi]$, $i \in \{1, 2, 3\}$. The potential energy $U(\mathbf{q}_{\mathbf{g}})$ is stored in the springs. It can hence be written as

$$\begin{aligned}
U(\mathbf{q}_{\mathbf{g}}) &= \frac{1}{2} [K_{12}(L_{12} - l_{012})^2 + K_{23}(L_{23} - l_{023})^2 \\
&\quad + K_{34}(L_{34} - l_{034})^2 + K_{14}(L_{14} - l_{014})^2]
\end{aligned} \tag{5}$$

with K_{ij} and l_{0ij} respectively the stiffness and the free-length of the spring attached between nodes A_i and A_j . The set of joint coordinates \mathbf{q} depends on the actuation mode. The different expressions are provided in Table 2.

3.3. Modeling of CA

For a Cable-Actuated Snelson cross (CA), two springs out of four are replaced by non-elastic cables (Fig. 2) thus generating four possible set-ups. The joint coordinates $\mathbf{q} = [\rho_1, \rho_2]^T$ are represented in Fig. 2. The mechanisms present only one unconstrained DoF [2, 6] which preserves compliance. Thus, $q_u \in \mathbb{R}$. The selected coordinate depends on the position of actuated cables, as reported in Table 3 which also contains the derived models. The rotation matrix \mathbf{R}_{θ_i} is

$$\mathbf{R}_{\theta_i} = \begin{bmatrix} \cos(\theta_i) & -\sin(\theta_i) \\ \sin(\theta_i) & \cos(\theta_i) \end{bmatrix} \tag{6}$$

TM	CA1	CA2
q_u	L_{14}	L_{12}
\mathbf{q}	$\rho_1 = L_{12}, \rho_2 = L_{34}$	$\rho_1 = L_{14}, \rho_2 = L_{23}$
$\Phi(\mathbf{q}_g)$	$\cos(\theta_1) = \frac{L_{13}^2 + q_u^2 - \rho_2^2}{2L_{13}q_u}$	$\cos(\theta_1) = \frac{\rho_1^2 + q_u^2 - L_{24}^2}{2q_u\rho_1}$
	$\cos(\theta_2) = \frac{\rho_1^2 - L_{24}^2 - q_u^2}{2L_{24}q_u}$	$\cos(\theta_4) = \frac{\rho_2^2 + q_u^2 - L_{13}^2}{2\rho_2q_u}$
	$A_1 = \left[-\frac{q_u}{2} \ 0\right]^T$	$A_1 = \left[-\frac{\rho_1}{2} \ 0\right]^T$
	$A_4 = -A_1$	$A_4 = -A_1$
	$A_2 = A_4 + \mathbf{R}_{\theta_2} [L_{24} \ 0]^T$	$A_2 = A_1 + \mathbf{R}_{\theta_1} [q_u \ 0]^T$
$A_3 = A_1 + \mathbf{R}_{\theta_1} [L_{13} \ 0]^T$	$A_3 = A_2 + \mathbf{R}_{\theta_1}\mathbf{R}_{\theta_4} [-\rho_2 \ 0]^T$	
$U(\mathbf{q}_g)$	$\frac{1}{2} [K_{23}(L_{23} - l_{023})^2 + K_{14}(q_u - l_{014})^2]$	$\frac{1}{2} [K_{12}(q_u - l_{012})^2 + K_{34}(L_{34} - l_{034})^2]$

TM	CA3	CA4
q_u	θ_1	L_{14}
\mathbf{q}	$\rho_1 = L_{14}, \rho_2 = L_{12}$	$\rho_1 = L_{12}, \rho_2 = L_{23}$
$\Phi(\mathbf{q}_g)$	$\cos(\theta_3) = \frac{\rho_1^2 + \rho_2^2 - L_{24}^2}{2\rho_1\rho_2}$	$\cos(\theta_3) = \frac{q_u^2 + \rho_1^2 - L_{24}^2}{2q_u\rho_1}$
	$A_1 = \left[-\frac{\rho_1}{2} \ 0\right]^T$	$\cos(\theta_4) = \frac{\rho_1^2 + \rho_2^2 - L_{13}^2}{2\rho_1\rho_2}$
	$A_4 = -A_1$	$A_1 = \left[-\frac{q_u}{2} \ 0\right]^T$
	$A_2 = A_1 + \mathbf{R}_{\theta_3} [\rho_2 \ 0]^T$	$A_4 = -A_1$
	$A_3 = A_1 + \mathbf{R}_{\mathbf{q}_u} [L_{13} \ 0]^T$	$A_2 = A_1 + \mathbf{R}_{\theta_3} [\rho_1 \ 0]^T$
$A_3 = A_2 + \mathbf{R}_{\theta_3}\mathbf{R}_{\theta_4} [-\rho_2 \ 0]^T$	$A_3 = A_2 + \mathbf{R}_{\theta_3}\mathbf{R}_{\theta_4} [-\rho_2 \ 0]^T$	
$U(\mathbf{q}_g)$	$\frac{1}{2} [K_{23}(L_{23} - l_{023})^2 + K_{34}(L_{34} - l_{034})^2]$	$\frac{1}{2} [K_{34}(L_{34} - l_{034})^2 + K_{14}(q_u - l_{014})^2]$

Table 3: Modeling of Cable-Actuated Snelson cross (CA) depending on the cable locations (see Fig. 2)

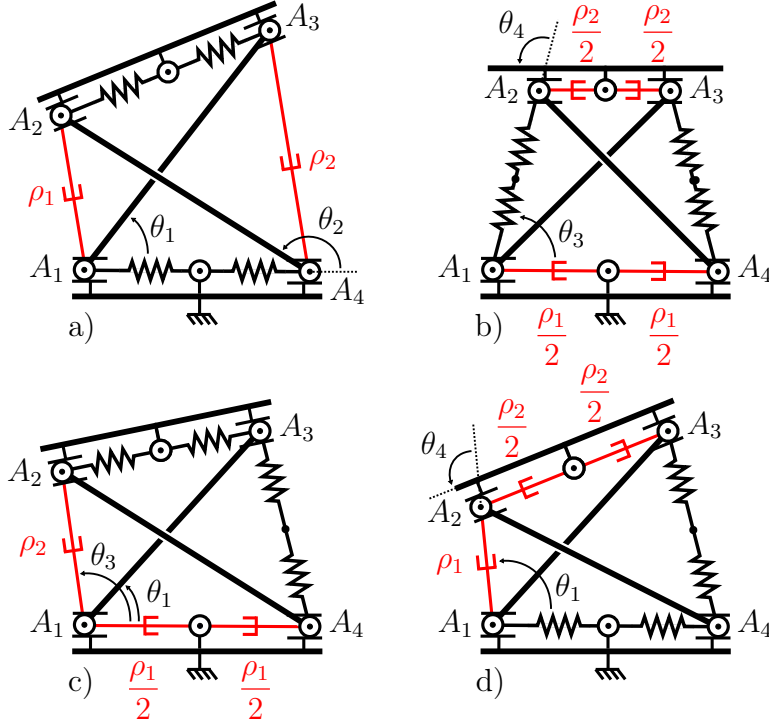


Figure 2: Cable-actuated SC with actuators in red a) CA1, b) CA2, c) CA3 and d) CA4

3.4. Computation of the tensegrity configuration

In [4, 38], tensegrity configurations have been analytically determined for SC with zero free-length springs. When non-zero free-length springs are considered, numerical analysis is considered [6, 9]. Here, TM possess up to four springs with non-zero free-lengths. No analytic solution can then be derived to the authors' knowledge. A numerical approach is then chosen to determine configurations.

A tensegrity configuration is computed for a given set of joint coordinates \mathbf{q} . The expression of the potential energy $U(\mathbf{q}_g)$ derived in (5) and Tab. 3 is obtained taking into account the loop closure equations. It is thus not needed to verify these constraints explicitly. Rather than using constrained optimization methods [9] which would lead to large computation times, we follow a 4-step sequential approach:

1. Zero of the first derivative of $U(\mathbf{q}_g)$ with respect to \mathbf{q}_u is computed.
2. The mechanical stability of the obtained configuration is verified by computing the second derivative of $U(\mathbf{q}_g)$ with respect to \mathbf{q}_u and checking it is a **positive definite** matrix.
3. The internal forces are computed and the tensions of the tensile elements are verified.

4. The conditions $\theta_1, \theta_2, \theta_3, \theta_4 \in [0, \pi]$ and $A_{1x} < A_{4x}$ are finally verified to respect assembly limits and avoid mirrored configurations with respect to the x axis and the y axis respectively.

The internal forces are computed using static equilibrium equations at the nodes of the TM. For sake of clarity, the dependence of static equations to the coordinates \mathbf{q}_g is omitted in the following. With \mathbf{A}_n and \mathbf{A}_e the equilibrium matrices usually used to describe a tensegrity [2] and which **depend on the pose** of the mechanical elements, the norms of the internal forces \mathbf{t}_n and \mathbf{t}_e for the non-elastic and elastic elements respectively are linked by equation (7).

$$\mathbf{A}_n \mathbf{t}_n + \mathbf{A}_e \mathbf{t}_e = \mathbf{0} \quad (7)$$

After step 2, the node coordinates are known. Then, the pose of the mechanical elements is known and thus, \mathbf{A}_n and \mathbf{A}_e can be computed. The length of the elastic elements can also be determined and knowing their mechanical parameters, \mathbf{t}_e is computed. Therefore, all terms in (7) are known except \mathbf{t}_n . The forces in the bars and cables can then be computed as

$$\mathbf{t}_n = -\mathbf{A}_n^{-1}(\mathbf{A}_e \mathbf{t}_e) \quad (8)$$

To compute the internal forces of all proposed SC, five different sets of static equilibrium equations are considered; one for each cable-actuated SC and one for SCs with four springs. Their expressions are given in AppendixB.

4. Performance criteria

To evaluate the behavior of TM, standard criteria such as the workspace are defined as well as specific information for these self-stressed structures such as potential energy and internal forces.

4.1. End-effector workspace

It is well known that TM can present multiple stable configurations [35] for a given set of joint variables \mathbf{q} . Their determination was for instance considered in [6]. However, these configurations may not be reachable without the use of an external load. We then prefer to consider the end-effector workspace as the set of all the poses than can be reached from an initial state by integration of infinitesimal variations of \mathbf{q} . The selection of \mathbf{q} is here carried out using a consistent approach which follows the proposed algorithm in AppendixC.

When a mechanism is assessed considering only one actuation mode, the end-effector workspace is usually determined for given ranges of joint variables. These ranges can be selected either with respect to a given application [9] or by determining them from the assembly limits [4]. In our situation, we wish to compare different actuation modes. They can be of different physical nature, with modification of spring stiffness or cable length for instance. Having a fair comparison is then not straightforward and it would not make sense to use the same numerical values to bound variables of different physical meanings. Moreover, the behavior of TM is intrinsically linked to the motion of their tensile elements which have a maximum elongation to prevent failure. Our proposition is then to set ranges as limits in the elongation of these elements, and keep their variations identical between the different actuation modes. In other words, we define the joint workspace as all values of \mathbf{q} ensuring that the elongation d_e of a spring remains between some minimal and maximal elongations, denoted respectively as $\delta_{e_{min}}$ and $\delta_{e_{max}}$. The end-effector workspace \mathbf{W}_e is then defined as below, with n the number of springs in the mechanism and $i \in [1, n]$.

$$\mathbf{W}_e = \left\{ \mathbf{x}(\mathbf{q}_g) \mid \begin{array}{l} \Phi(\mathbf{q}_g) = \mathbf{0} \\ \frac{\partial U(\mathbf{q}_g)}{\partial \mathbf{q}_u} = \mathbf{0} \\ \frac{\partial^2 U(\mathbf{q}_g)}{\partial \mathbf{q}_u^2} > \mathbf{0} \\ \mathbf{t}_t(\mathbf{q}_g) > \mathbf{0} \\ \delta_{e_{min}} \leq d_{e_i}(\mathbf{q}_g) \leq \delta_{e_{max}} \end{array} \right\} \quad (9)$$

4.2. Manipulability

The ability of a mechanism to generate velocities varies throughout its workspace. The knowledge of these variations is critical for the evaluation of a mechanism and its control. In particular, the presence of singularities, where velocities cannot be generated along some directions, must be identified. In our context, only two DoF of the end-effector can be independently controlled and the last one corresponds to the mechanism compliance. To compute the ability to generate velocities, we therefore consider controlled translations $\dot{\mathbf{g}} = \vec{\mathbf{v}}$ and compliant rotation $\dot{\varphi}$. With $\dot{\mathbf{q}} = [\dot{\rho}_1, \dot{\rho}_2]^T$, the actuators velocities, the controlled translations are written as

$$\vec{\mathbf{v}} = \mathbf{J}_d \dot{\mathbf{q}} \quad (10)$$

with $\mathbf{J}_d = \frac{\partial \mathbf{g}}{\partial \mathbf{q}}$ the 2×2 kinematic Jacobian.

Multiple indices as the conditioning number of \mathbf{J}_d or the manipulability can be used for this analysis. Here, we desire a global criterion to represent the mechanism capabilities and also the distance to a singular configuration. We then choose the manipulability measure μ , as computed in [40, 26, 28]. It is computed for each \mathbf{x} in the end-effector workspace with the following expression.

$$\mu = \sqrt{\det(\mathbf{J}_d \mathbf{J}_d^T)} \quad (11)$$

A usual drawback of the manipulability measure is that it can give inapplicable interpretations if a dimensionally non-homogeneous Jacobian matrix is obtained [26]. It is however not the case here as only translation velocities are considered. For a stiffness actuated SC, $\partial \mathbf{q}$ represents a stiffness variation. For the other SCs, it represents a length variation of a bar, a spring free-length or a cable length. When comparing the manipulability values, special care must then be taken as order of magnitudes may differ between a SA and the other SCs. Finally, when specific manipulability maps are encountered, the singular values of \mathbf{J}_d can be computed to better understand the behavior of the mechanism along each direction x and y .

4.3. Level of potential energy

Tensegrity Mechanisms (TM) are self-stressed mechanisms and therefore present a non-zero potential energy at rest. This potential energy may be desired minimal to lower the energy needed to perform motions, which is also in favor of safety if interactions with humans are expected. Conversely, high potential energy can be of interest if it is used to carry out a task such as TM initial deployment, as described in [24], or when bursts of energy are needed [20]. The evaluation of potential energy stored in a TM is then of interest in our assessment. The potential energy is stored in the springs for the TM under study. Its expression was formulated for all TM in Section 3 and its value is computed for each pose \mathbf{x} in the end-effector workspace.

4.4. Internal forces

The self-stress property of TM also means that an equilibrium configuration is obtained thanks to non-zero internal forces. These forces have an impact on the TM design as the TM elements must be sized accordingly. Analysis of the internal forces is then critical from a design point of view. Three kinds of elements are used in the proposed TM: bars, springs and cables. Here we consider that all elements of a same kind have a same maximal sustainable force and we then propose to analyze the maximal force applied to all elements of a same type in a given TM.

Then, the maximal values of forces F_b , F_s and F_c applied respectively to the bars, springs and cables are determined for each pose \mathbf{x} in the end-effector workspace using the method exposed in Section 3.4.

5. Results and discussion

In this section, the methods implemented for the computation of the results and the generation of the maps are firstly given. Second, in order to help the design of complex tensegrity mechanisms based on Snelson crosses, results of interest are discussed. Rather than trying to comment all the obtained information, which would be at some point dependent on the task under consideration, the most significant results are outlined and listed. The reader may then refer to the performance of interest to get information on adequate designs.

5.1. Generation of performance maps

In the chosen numerical implementation, the expression of $U(\mathbf{q}_g)$, its first and second derivatives were derived analytically with the Symbolic Math ToolboxTM. The obtained expressions are displayed in [12].

To compute the zero of the first derivative of $U(\mathbf{q}_g)$, *i.e.* Step 1 in Section 3.4, an iterative minimization method is chosen. A Newton-Raphson algorithm is used for its ease of implementation, although other numerical methods might be used as well. If the chosen numerical method does not converge, the configuration would be considered as not valid. Non-convergence was observed only on isolated cases, that were outside the workspace boundaries. The Jacobian matrix involved in the Newton-Raphson algorithm is denoted \mathbf{J}_u , with the term $\mathbf{J}_{u_{ij}}$ on the i -th row and j -th column expressed as

$$\mathbf{J}_{u_{ij}} = \frac{\partial^2 U(\mathbf{q}_g)}{\partial q_{u_i} \partial q_{u_j}} \quad (12)$$

The Newton-Raphson algorithm requires an initial guess which is the solution of (2). We use the square-shaped configuration of the SC obtained when both bars have the same length L , springs of identical properties and length of tensile elements is $L/\sqrt{2}$.

To compute the manipulability presented in Section 4.2, the kinematic Jacobian \mathbf{J}_d must be determined. Here, it is computed numerically using a centered finite differences method.

The performance criteria are computed for each set of joint coordinates of the thirteen mechanisms. The algorithm presented in AppendixC is used to determine all reachable configurations as defined in Section 4.1. Different sets of joint coordinates can correspond to a same tensegrity configuration [10]. The performances are thus displayed in both operational and joint workspaces. Moreover, to ease the understanding of manipulability maps of SA, a logarithmic scale is used.

A bar length of 100 mm is chosen. A spring free-length l_0 of 50 mm is selected and boundaries on the elastic length of the springs $\delta_{e_{min}} = 5$ mm and $\delta_{e_{max}} = l_0$ are used

to ensure that the initial square-shaped configuration is a tensegrity configuration. The spring stiffness is chosen equal to 20 N/m.

All the computed performance maps are tabulated and available in the enclosed *pdf* file to this paper. The dataset used to display these maps is available in [12].

To help the analysis of the performance maps, several tensegrity configurations are displayed on top of the maps with the bars in solid lines, the actuated tensile elements in dotted lines and the passive ones in dashed lines, the nodes with point-shaped markers and the point \mathbf{g} with a diamond-shaped marker.

5.2. Kinematic behavior

Three specific motions can be identified from the observation of the end-effector workspaces. The first one is illustrated in Fig. 3 for BA where the end-effector remains parallel to the base of the SC in its whole workspace. This is of interest to get position modulation of the end-effector. The second motion is obtained when tensile elements are actuated in M2 configuration (See Table 1 for M_i definition). A 1-D translation is obtained as illustrated in Fig. 4. The mechanism offers a behavior equivalent to a linear actuator. Finally, large reconfiguration in orientation of the end-effector are observed with M1, M3 and M4. In particular M1 offers the largest angular range (Fig. 5) with positive or negative orientations compared to M3 and M4 where the workspace asymmetry is very clear (Fig. 6).

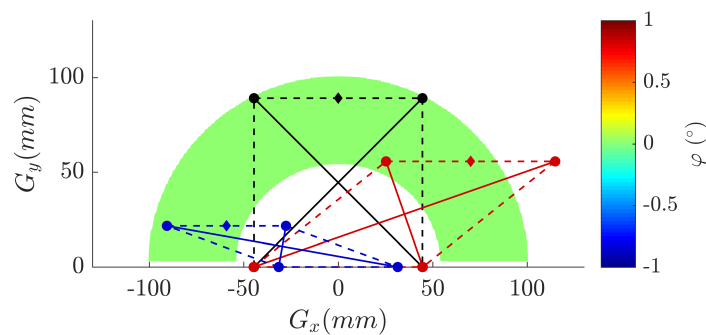


Figure 3: End-effector workspace obtained for BA.

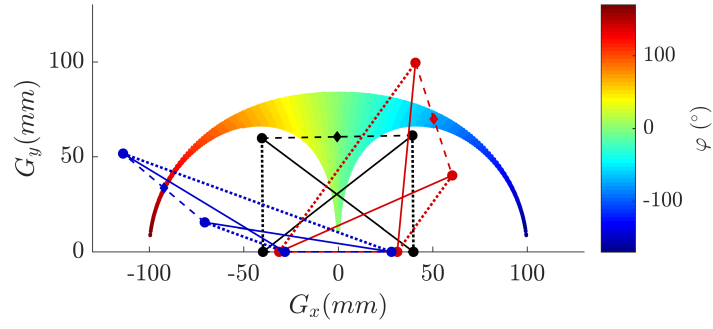


Figure 5: End-effector workspace obtained for FA1.

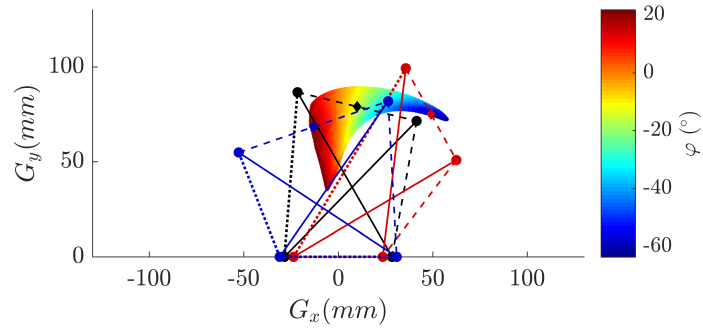


Figure 6: End-effector workspace obtained for FA3.

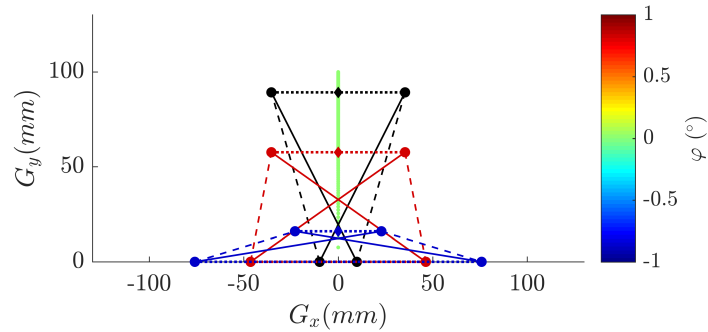


Figure 4: End-effector workspace obtained for CA2.

These observations show that the end-effector motions strongly depend on the

Actuator position	Actuator stroke			End-effector stroke			
	FA (mm)	SA (N/m)	CA (mm)	Unit	FA	SA	CA
M1	150	103	192	(°)	340	74	342
M2	150	103	192	(mm)	94	28	92
M3 & M4	106	333	107	(°)	85	66	107

Table 4: Actuator and end-effector strokes obtained for each TM.

position of the actuators. However, for the second and the third highlighted situations, the range of motion is also a function of the type of actuation. To evaluate these motion ranges we define as the end-effector stroke the maximum translation range for M2, and the maximum angular range for M1, M3 and M4. The evaluation of these indicators is reported in Table 4 with the joint strokes. It appears clearly that FA and CA are best suited for large range of motions. However, FA possesses a better ratio between actuator stroke and end-effector stroke. In other words, it is the best solution if the largest motion for a given actuator stroke is searched for.

The results with SA need to be considered with special attention as manipulability presents large variations. As shown in Fig. 7, large manipulability values are obtained when a SA is deployed. On the opposite, very low manipulability is obtained when it is folded. The variations are substantial so that a logarithmic scale is needed to reflect the variations. This means that large variations of the joint coordinates will generate a small motion where the manipulability is low. Figure 8 illustrates this behavior by displaying the maximum actuator position needed to reach a given configuration over the workspace of SA1. It shows that only 50% of the actuator stroke including the minimal joint coordinate is needed to reach more than 90% of the motion range with the full actuator stroke. When considering stiffness-actuated mechanisms, the strokes must be carefully chosen as an increase of the actuated spring stiffness may not lead to a substantial increase of the workspace.

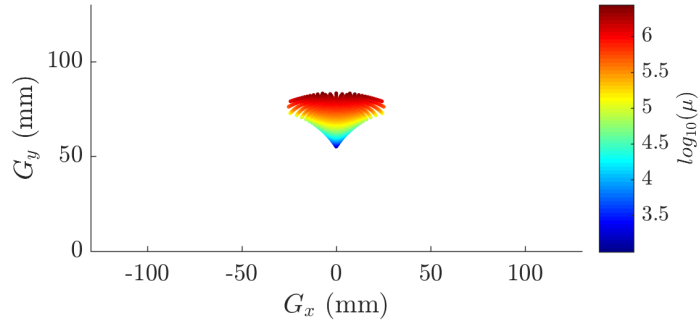


Figure 7: Manipulability obtained for SA1.

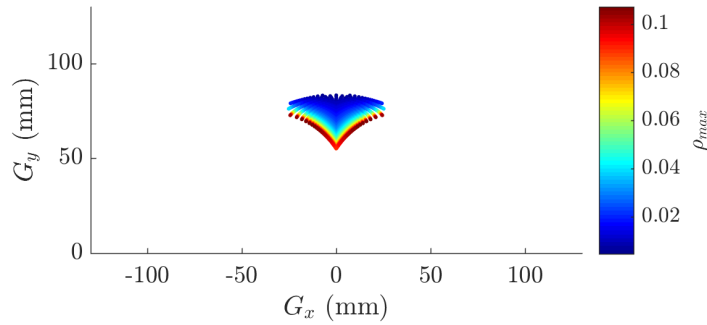


Figure 8: Maximum actuator position needed for each configuration of the workspace for SA1

Further analysis of the manipulability variations also leads to notice interesting results as the ones obtained for BA. For this mechanism, a constant manipulability of 0.5 is obtained in the whole workspace (Fig. 9). The singular values of the kinematic Jacobian matrix are computed and have values of 1 (resp. 0.5) along direction x (resp. y). It means that for constant actuator velocities the speed of the end-effector do not fluctuate which may be convenient for control and controller synthesis.

SC	FA1	FA3	FA4	CA1	CA3	CA4
$\bar{\mu}$	0.23	0.14	0.15	0.32	0.38	0.34
μ_{max}	0.28	0.34	0.30	0.76	2.74	0.73

Table 5: Average and maximal manipulability for the FA and CA. M2 not considered as $\mu \approx 0$.

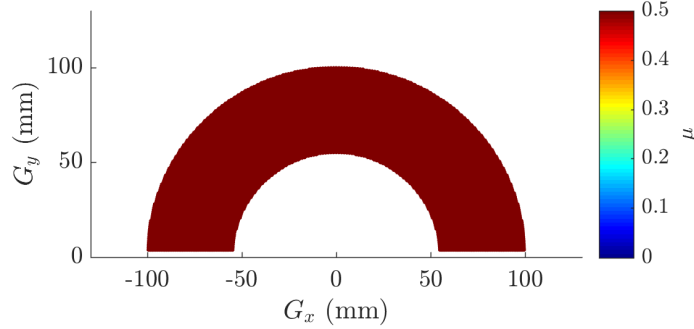


Figure 9: Manipulability obtained for BA.

M2 having only 1-DoF with a translation motion along y , velocities can not be generated along x . Therefore, the manipulability should be null in the whole workspace. Some very small values of μ can be noticed on the maps due to rounding errors with the conducted numerical analysis.

Finally, FA and CA are similar mechanisms in terms of workspace and actuation as in practical implementations the free-length control is usually carried out by adjusting the length of a cable. However, as shown in Table 5 the manipulability is significantly different with larger average and maximum values for CA. In a same way, maps indicate that M3 and M4 have close performances in terms of workspace. However, manipulability variations are different especially for free-length actuated SCs where high value of manipulability is not located in the same area of the workspace, as shown in Fig. 10 and Fig. 11. During the design, the obtained manipulability can then be a determining factor to select the best suited actuation mode.

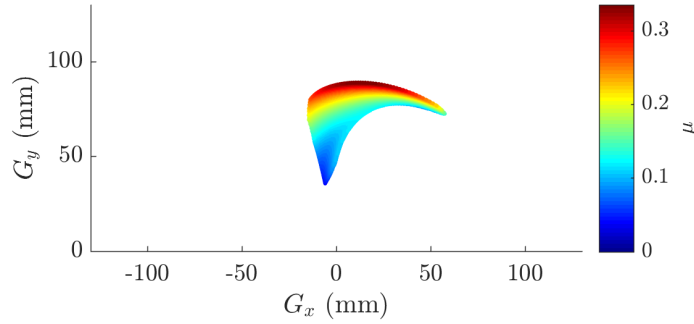


Figure 10: Manipulability obtained for FA3.

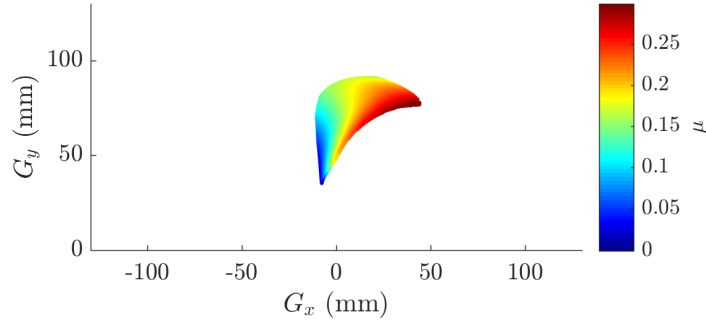


Figure 11: Manipulability obtained for FA4.

5.3. Potential energy optimization

5.3.1. Potential energy minimization

To minimize the energy needed to perform a task, or to ensure safe interactions, it is of interest to minimize the potential energy. As a synthesis of the map representing the potential energy, the average value in the whole workspace is computed for each TM. The values are reported in Table 6. M1 and M2 possess the same average potential energy, as they can be considered as similar mechanisms after a 90° rotation. The same observation can be done for M3 and M4. The results show that the bar-actuated SC has the highest potential energy. For M1 and M2, the free-length actuated SC presents the lowest average potential energy while the cable-actuated one presents the minimal energy for M3 and M4. However, for M1 and M2 the maximum potential energies within the workspace are similar for FA and CA with

Actuator position	FA	SA	CA	BA
M1 & M2	38.3	41.4	51.2	
M3 & M4	38.0	69.5	18.7	
L_{13} and L_{24}				88.8

Table 6: Average potential energy in mJ obtained for each TM. In green the minimal row value.

respectively 99 and 100 mJ, whereas the maximal ones for M3 and M4 are of 145 mJ for FA and 94 mJ for CA. In conclusion, FA and CA are the best suited mechanisms for potential energy minimization. Choosing between FA and CA depends on the needs, *i.e.* if it is more relevant to minimize the average energy or the highest value of energy.

5.3.2. Potential energy maximization

Potential energy maximization is desired if a TM is to be deployed without effort. Actuation is then used to fold the mechanism before the self-deployment. M1 is interesting as the highest levels of energies are obtained when the TM is folded, as illustrated in Fig. 12. Conversely, high levels of potential energy are reached for BA and M2 when the TM is already deployed as shown in Fig. 13. Similarly, M3 and M4 do not have a high potential energy when folded but for a deployed configuration with positive orientation depicted in black in Fig. 14. Thus, BA, M2, M3 and M4 mechanisms are not the best-suited solutions for self-deployment.

During deployment, the end-effector of TM will follow the direction defined by the maximum gradient of potential energy. It is interesting to note that such direction depends on the TM selection and its initial configuration. For instance, the use of the configurations displayed in Fig. 12 will lead to a vertical motion, while the ones in Fig. 14 will mainly cause a rotation. A wide range of paths can also be obtained with the same mechanism. For instance, linear motions with different directions can be obtained with the BA in Fig. 12 by changing the configuration before release, *i.e.* the one represented in black. Such behavior is here analysed with quasi-static hypotheses. The impact of dynamics would then need to be included for further analysis. Finally, BA possesses the highest average potential energy with 88.8 mJ making it the most interesting mechanism amongst the ones proposed for large energy releases.

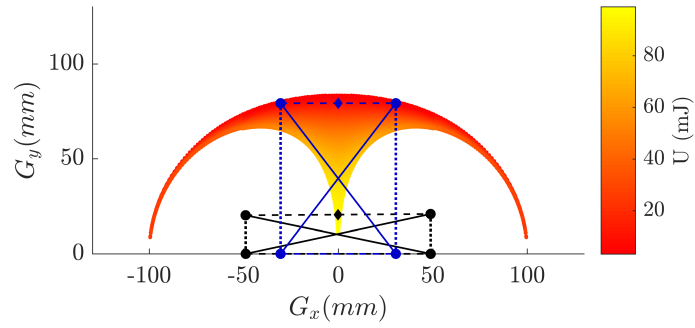


Figure 12: Potential energy of FA1 with the high energy configuration in black (horizontal one) and the low one in blue (vertical one)

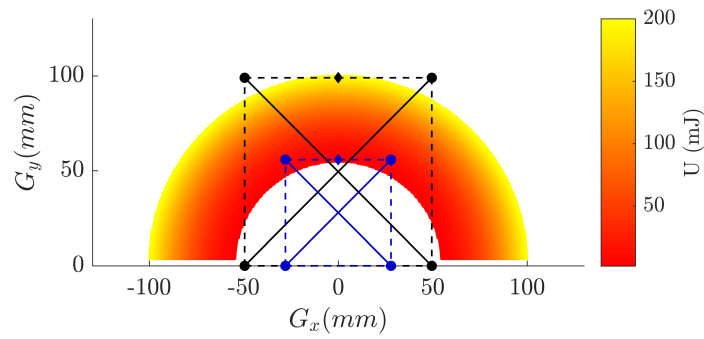


Figure 13: Potential energy of the bar-actuated SC with the high energy configuration in black (large SC) and the low one in blue (small SC).

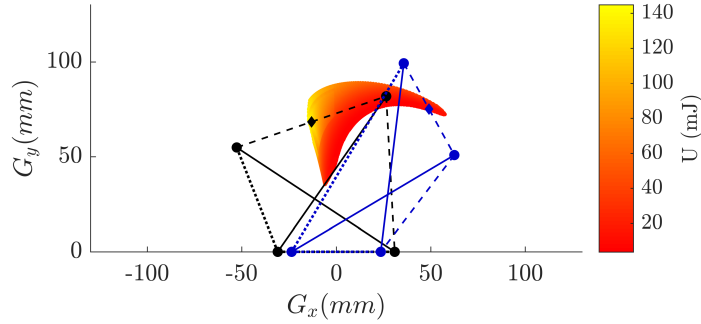


Figure 14: Potential energy of FA3 with the high energy configuration in black (SC tilted to the left) and the low one in blue (SC tilted to the right).

5.4. Evolution of internal forces

For design purposes, minimal internal forces are usually looked for. In Table 7 the average and maximal forces for each TM are summarized. Results show that even if the average value over the workspace is low, high maximal forces can be encountered, as observed for instance with CA3. The opposite behavior can also be identified: In the case of SA1, the average forces are the highest among all TM for a given set of actuator positions, but the maximal forces are the lowest. These observations can be explained by the high forces required to reach some specific areas of the workspace as illustrated for CA3 in Fig. 15, with in black the corresponding configuration. These cases do not correspond to quasi-singular configurations or assembly limits, but to configurations where the springs elongations are the largest. This shows the importance of a specific study of internal forces during the synthesis of a TM, as areas involving high internal forces can be easily avoided.

Considered TM	\overline{F}_b	\overline{F}_s	\overline{F}_c	$F_{b_{max}}$	$F_{s_{max}}$	$F_{c_{max}}$
BA	0.81	0.62		1.99	1.00	
FA1 & FA2	0.56	0.39		0.99	0.99	
SA1 & SA2	0.69	0.49		0.80	0.67	
CA1 & CA2	0.78	0.67	0.47	1.00	1.00	1.88
FA3 & FA4	0.56	0.39		1.24	0.99	
SA3 & SA4	1.27	0.92		1.99	1.69	
CA3 & CA4	0.57	0.37	0.43	3.28	1.00	2.92

Table 7: Average and maximal internal forces in the workspace of each TM. Values in N.

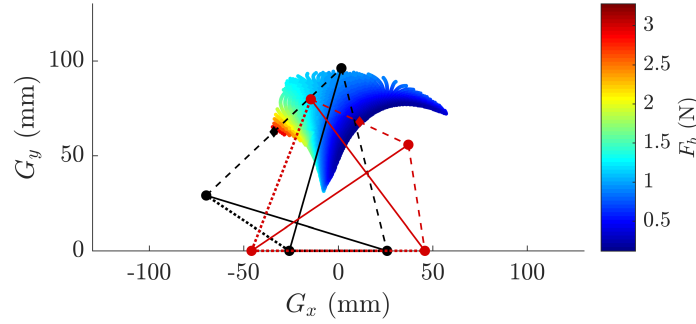


Figure 15: Maximal forces in the bars of CA3. In black and in red the configurations with the highest and the lowest internal forces in the bars.

For the M1 mechanisms, the computed maps indicate that the low internal forces are obtained when the structure is deployed. Moreover, the largest end-effector stroke defined in Section 5.2 is obtained when the tensegrity is in these configurations. It means that the motion capabilities of these tensegrities can be exploited while minimizing the internal forces. For M3 and M4, the same comments are valid but only for the rotational motion. On the other hand BA requires high internal forces to be able to reach deployed configurations. Therefore, depending on the desired maximal internal forces, the choice of actuation mode helps optimizing the obtained end-effector stroke.

Moreover, to design a structural element, the maximal compression or traction force is usually considered. From Table 7, we can see that the maximal force in the springs is lower or equal to the forces in the cables or the bars. This is convenient as it is easier to design bars and cables than springs with high maximal force.

Finally, bars have a high mass compared to the ones of the springs and the cables. To design a lightweight device it is then interesting to reduce their cross-section and thus reduce the compression forces. In Table 7, we can observe that the maximal forces in the bars are lower when exploiting M1 than M3 or M4. In addition to the larger workspace, M1 is then also more interesting than M3 or M4 to achieve rotation motions while minimizing the mass of the TM.

6. Building blocks

Mechanisms are often designed to achieve a motion which is task-specific. Therefore, the kinematics of the system are usually the first and most desired property. From the previous results, TM with specific motions can interestingly be identified in order to create building blocks, to be used as the equivalent of conventional joints. Such a building block approach was indeed shown to be of interest in the design of conventional robots or compliant mechanisms [16]. Mechanisms exclusively composed of TM or with hybrid architectures combining TM and conventional joints [13] can be elaborated using existing kinematic schemes. Thus, the design of the mechanism can be carried out starting from desired motions. Three building blocks are identified for that based on their kinematics and proposed in Table 8. Block designation, reference TM designation and representation of the TM architecture provided. For all of them, the stiffness can be tuned by design, with the choice of the springs or by control of elastic elements.

The first block is the prismatic SC. It carries out a 1-DoF motion, so it is equivalent to a prismatic joint along y axis. Its implementation was considered with actuators on top and bottom sides. A simplified implementation is also possible with only one of the two actuators. The range of motion is then reduced.

The second block is the XY SC. It is equivalent to a XY table, *i.e.* two serially-connected perpendicular prismatic joints. With such a TM, position control in the plane is possible with a constant orientation of the end-effector. Thanks to the use of two actuators, both position coordinates can be independently controlled.

The third block is the 2-DoF planar SC. It allows planar motions of the end-effector with two independent possible motions. Among possible TM, M1 was identified as the one with the most interesting workspace and internal forces. It can be used to set the orientation φ of the end-effector, and at the same time to set the position along the x direction, or the y direction, or along a prescribed path defined as a combination of x and y coordinates. These motions are obtained by control of the two actuators, with the possibility to get a wide choice of motions, from a rotation along a circle of adjustable radius to a translation along one direction combined with orientation modification.

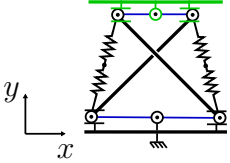
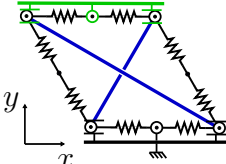
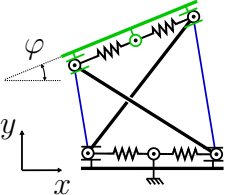
Block designation	Considered TM	TM architecture
Prismatic SC	M2	
XY SC	BA	
2-DoF Planar SC	M1	

Table 8: Proposed building blocks and their representation. In blue the actuated elements in each TM and in green the end-effector.

The results observed in Section 5 about the potential energy, the manipulability and the internal forces can then be exploited to choose the actuator type and the actuator strokes, which are best suited for the desired task. For the Prismatic SC and the 2-DoF Planar SC, the main results from Section 5 that can be exploited for the choice of the actuator type are tabulated in Table 9. These comparisons are elaborated considering the achievable performances in the whole workspace of each SC. They must then be used carefully if the design is achieved for a specific range of end-effector pose.

These building blocks can now be assembled to design new mechanisms. Their specific kinematic behaviors allow to aim for a systematic design method of tensegrity-based compliant manipulators, in analogy with the design of rigid conventional robots.

Performance index	Comparison
Workspace size	CA > FA > SA
End-effector stroke	CA \approx FA > SA
Ratio between end-effector stroke and actuator stroke	FA > CA (SA NC)
Manipulability (2-DoF planar SC)	CA > FA (SA NC)
Average potential energy	CA > FA \approx SA
Maximal force in the bars	FA \approx CA > SA
Maximal force in the springs	FA \approx CA > SA

Table 9: Conclusions for the choice of actuator type of the Prismatic SC and the 2-DoF Planar SC. The operator $A > B$ designate higher values of the mechanism A compared to mechanism B in its whole workspace for the performance index considered in the table row. NC means Not Compared due to different physical quantities.

7. Conclusions and perspectives

In this paper, the influence of actuation modes on SC was assessed. Performance criteria were firstly proposed to characterize the behavior of TM. A numerical study of the thirteen different mechanisms obtained using four distinct actuation types was then carried out. One perspective of this work would be to determine the most adequate method for this kind of numerical analysis, given the specific formulation of the equilibrium determination.

The performance criteria were computed for each actuation mode to generate performance maps helping comparing the mechanisms. These maps showed that actuation type and position can widely change the behavior of a SC and also lead to interesting properties. The most interesting results were extracted and building blocks were identified to be used in SC assemblies in analogy with conventional robot design. Thanks to the wide variety of behaviors obtained with a simple TM, this paper shows the complexity and large possibilities of tensegrity-based robots. Other behaviors could probably be obtained if hybrid actuation **or non identical passive elements are considered**. This constitutes the second perspective of this work.

The approach we developed for the SC could also be applied to other tensegrity structures, either planar or also with spatial arrangements. This would help to enlarge the library of TM of interest as robot components, and thus the possibilities in the design of tensegrity-based robots.

Acknowledgement

This work is part of Multiflag project (ANR-16-CE33-0019) funded by the French National Research Agency (ANR) and supported by Investissements d’Avenir pro-

gram (Labex CAMI & Equipex ROBOTEX) under references ANR-11-LABX-0004, ANR-10-EQPX-44 and the Grand Prix Scientifique 2018, Fondation Charles Deforey, Institut de France.

Appendix A. Notations

Symbol	Designation
\mathbf{A}_e	Equilibrium matrix of elastic elements
\mathbf{A}_n	Equilibrium matrix of non-elastic elements
A_i	i -th node
$\delta_{e_{min}}, \delta_{e_{max}}$	Boundary values of spring elongation
d_{e_i}	Elongation of the i -th spring
F_b, F_s, F_c	Internal forces respectively in bars, springs and cables
$\mathbf{g} = [G_x, G_y]^T$	Position of the end-effector centroid
$\dot{\mathbf{g}} = \dot{\mathbf{v}}$	Velocities of the end-effector centroid
\mathbf{J}_d	Kinematic Jacobian matrix
\mathbf{J}_u	Jacobian matrix associated to the Newton-Raphson method
K_{ij}	Stiffness of the spring attached to nodes A_i and A_j
L_{ij}	Distance between nodes A_i and A_j
$l_{0_{ij}}$	Free-length of the spring attached to nodes A_i and A_j
μ	Manipulability
n	Number of springs in the mechanism
φ	Orientation of the end-effector
$\dot{\varphi}$	Angular velocity of the end-effector
Φ	Loop closure equations
\mathbf{q}	Joint coordinates
$\dot{\mathbf{q}}$	Joint velocities
\mathbf{q}_g	Generalized coordinates
\mathbf{q}_u	Unconstrained coordinates
\mathbf{R}	Rotation matrix
θ_i	Orientation of structural elements
\mathbf{t}_e	Tensions in elastic elements
\mathbf{t}_n	Forces in non-elastic elements
\mathbf{t}_t	Tensions in tensile elements
U	Potential energy
\mathbf{x}	Pose of the end-effector
\mathbf{W}_e	End-effector workspace

Table A.10: List of symbols and their meanings

Acronym	Designation
BA	Bar-Actuated Snelson cross
CA	Cable-Actuated Snelson cross
FA	Free-length-Actuated Snelson cross
SA	Stiffness-Actuated Snelson cross
M_i	i - th set of actuator position (see Table 1)
CA_i	Cable-Actuated Snelson cross with i -th set of actuator position
FA_i	Free-length-Actuated Snelson cross with i -th set of actuator position
SA_i	Stiffness-Actuated Snelson cross with i -th set of actuator position
DoF	Degree of Freedom
TM	Tensegrity Mechanism
SC	Snelson Cross
SMA	Shape Memory Alloy

Table A.11: List of acronyms and their meanings

AppendixB. Derivation of internal forces

When four springs are used as tensile elements, the unknowns are the compression forces in the bars denoted F_{b13} and F_{b24} . The tension F_{sij} of the spring attached to nodes A_i and A_j is computed using the node positions. The vector \mathbf{e}_{ij} is a unit vector giving the direction of the element attached to nodes A_i and A_j . The following expressions are determined by expressing the static equilibrium at nodes A_2 or A_3 along x axis.

$$\underbrace{\begin{bmatrix} e_{42x} & 0 \\ 0 & e_{13x} \end{bmatrix}}_{\mathbf{A}_n} \underbrace{\begin{bmatrix} F_{b13} \\ F_{b24} \end{bmatrix}}_{\mathbf{t}_n} + \underbrace{\begin{bmatrix} e_{21x} & 0 & e_{23x} \\ 0 & e_{34x} & e_{32x} \end{bmatrix}}_{\mathbf{A}_e} \underbrace{\begin{bmatrix} F_{s12} \\ F_{s34} \\ F_{s23} \end{bmatrix}}_{\mathbf{t}_e} = \mathbf{0} \quad (\text{B.1})$$

For the cable-actuated SCs, there are four unknowns, the compression forces in the bars and the tensions in the cables, with F_{cij} the tension in the cable attached to nodes A_i and A_j . The expressions are tabulated in Table B.12.

SC	Nodes	\mathbf{A}_n	\mathbf{t}_n	\mathbf{A}_e	\mathbf{t}_e
CA1	A_2 A_3	$\begin{bmatrix} \mathbf{e}_{21} & \mathbb{0}_{2 \times 1} & \mathbb{0}_{2 \times 1} & \mathbf{e}_{42} \\ \mathbb{0}_{2 \times 1} & \mathbf{e}_{34} & \mathbf{e}_{13} & \mathbb{0}_{2 \times 1} \end{bmatrix}$	$[F_{c12} \ F_{c34} \ F_{b13} \ F_{b24}]^T$	$\begin{bmatrix} \mathbf{e}_{23} \\ \mathbf{e}_{32} \end{bmatrix}$	F_{s23}
CA2	A_1 A_2	$\begin{bmatrix} \mathbf{e}_{14} & \mathbb{0}_{2 \times 1} & \mathbf{e}_{31} & \mathbb{0}_{2 \times 1} \\ \mathbb{0}_{2 \times 1} & \mathbf{e}_{23} & \mathbb{0}_{2 \times 1} & \mathbf{e}_{42} \end{bmatrix}$	$[F_{c14} \ F_{c23} \ F_{b13} \ F_{b24}]^T$	$\begin{bmatrix} \mathbf{e}_{12} \\ \mathbf{e}_{21} \end{bmatrix}$	F_{s12}
CA3	A_1 A_2	$\begin{bmatrix} \mathbf{e}_{12} & \mathbf{e}_{14} & \mathbf{e}_{31} & \mathbb{0}_{2 \times 1} \\ \mathbf{e}_{21} & \mathbb{0}_{2 \times 1} & \mathbb{0}_{2 \times 1} & \mathbf{e}_{42} \end{bmatrix}$	$[F_{c12} \ F_{c14} \ F_{b13} \ F_{b24}]^T$	$\begin{bmatrix} \mathbb{0}_{2 \times 1} \\ \mathbf{e}_{23} \end{bmatrix}$	F_{s23}
CA4	A_2 A_3	$\begin{bmatrix} \mathbf{e}_{21} & \mathbf{e}_{23} & \mathbb{0}_{2 \times 1} & \mathbf{e}_{42} \\ \mathbb{0}_{2 \times 1} & \mathbf{e}_{32} & \mathbf{e}_{13} & \mathbb{0}_{2 \times 1} \end{bmatrix}$	$[F_{c12} \ F_{c23} \ F_{b13} \ F_{b24}]^T$	$\begin{bmatrix} \mathbb{0}_{2 \times 1} \\ \mathbf{e}_{34} \end{bmatrix}$	F_{s34}

Table B.12: Considered SC, nodes considered for static equilibrium expression, matrices and vectors used for the computation of internal forces.

AppendixC. Computation of performance maps

Algorithm 1 Computation of performance maps

```

1: endOfWorkspace := false
2: configurationFound := false
3: stateρ1 := decrease
4: stateρ2 := decrease
5: qg := qg0      ▷ qg0 the generalized coordinates of a given square-shaped SC
6: while endOfWorkspace = false do
7: |   ▷ Find equilibrium position using non-linear minimization algorithm
8: |   qg := solve (  $\Phi(\mathbf{q}_g) = 0, \frac{\partial U(\mathbf{q}_g)}{\partial \mathbf{q}_u} = 0$  )
9: |   ▷ Check the tensegrity configuration and the assembly limits
10: |  if  $\frac{\partial^2 U(\mathbf{q}_g)}{\partial \mathbf{q}_u^2} > 0$  & te(qg) > 0 & {θ1, θ2, θ3} ∈ [0, π] & A1x < A4x then
11: |  |   save qg                                ▷ Configuration in the workspace
12: |  |   configurationFound := true
13: |  |   [ρ1, stateρ1] := MODIFY(ρ1, stateρ1)
14: |  else                                       ▷ Workspace boundary reached
15: |  |   if configurationFound = false then
16: |  | |   endOfWorkspace := true
17: |  | else
18: |  | |   configurationFound := false
19: |  | |   stateρ1 := decrease
20: |  | |   ρ1 := ρ10                            ▷ Reset first actuator position with ρ10 ∈ qg0
21: |  | |   [ρ2, stateρ2] := MODIFY(ρ2, stateρ2)
22: |  | end if
23: |  end if
24: end while

```

```

1: function MODIFY( $\rho_i$  ,  $state_{\rho_i}$ )
2:   if  $state_{\rho_i} = decrease$  then
3:     Decrease  $\rho_i$ 
4:     if  $\rho_i < limit_{\rho_i}$  then
5:        $state_{\rho_i} := increase$ 
6:     end if
7:   else
8:     Increase  $\rho_i$ 
9:   end if
10:  return [ $\rho_i, state_{\rho_i}$ ]
11: end function

```

References

- [1] B. N. R. Abadi, M. Farid, and M. Mahzoon. Introducing and Analyzing a Novel Three-Degree-of-Freedom Spatial Tensegrity Mechanism. *J. Comput. Nonlinear Dynam*, 9(2):021017–021017–8, February 2014.
- [2] M. Arsenault. *Développement et analyse de mécanismes de tensegrité*. PhD thesis, Université Laval, 2006.
- [3] M. Arsenault. Stiffness Analysis of a 2dof Planar Tensegrity Mechanism. *J. Mechanisms Robotics*, 3(2):021011–021011–8, April 2011.
- [4] M. Arsenault and C. M. Gosselin. Kinematic and static analysis of a planar modular 2-DoF tensegrity mechanism. In *IEEE International Conference on Robotics and Automation*, pages 4193–4198, May 2006.
- [5] M. Azadi, Saeed B., and G. Faulkner. A Variable Spring Using a Tensegrity Prism. *ASME Journal of Mechanisms and Robotics*, pages 35–43, January 2009.
- [6] J. Bayat and III Crane, C. D. Closed-Form Equilibrium Analysis of Planar Tensegrity Structures. *ASME. International Design Engineering Technical Conferences and Computers and Information in Engineering Conference*, 8(31):13–23, January 2007.
- [7] J. Begey, M. Vedrines, N. Andreff, and P. Renaud. Toward a design method for tensegrity-based medical robots. In *Surgetica: Computer-Assisted Medical Interventions. Scientific problems, tools and clinical applications.*, June 2019.

- [8] B. Bickel, S. Mani, B. Thomaszewski, and S. Coros. Modular Design of Complex Tensegrity Structures, January 2016.
- [9] Q. Boehler, I. Charpentier, M. Vedrines, and P. Renaud. Definition and Computation of Tensegrity Mechanism Workspace. *J. Mechanisms Robotics*, 7(4):044502–044502–4, November 2015.
- [10] Q. Boehler, M. Vedrines, S. Abdelaziz, P. Poignet, and P. Renaud. Influence of Spring Characteristics on the Behavior of Tensegrity Mechanisms. In *Advances in Robot Kinematics*, pages 161–169, June 2014.
- [11] Q. Boehler, M. Vedrines, S. Abdelaziz, P. Poignet, and P. Renaud. Toward an MR-compatible needle holder with adaptive compliance using an active tensegrity mechanism. In *Surgetica: Computer-Assisted Medical Interventions. Scientific problems, tools and clinical applications.*, December 2014.
- [12] [dataset], J. Begey, M. Vedrines, N. Andreff, and P. Renaud. Analytical expressions and performance data for the analysis of actuated snelson crosses. Mendeley Data, 2019.
- [13] J. M. Friesen, J. L. Dean, T. Bewley, and V. SunSpiral. A Tensegrity-Inspired Compliant 3-DOF Compliant Joint. In *IEEE International Conference on Robotics and Automation*, pages 1–9, May 2018.
- [14] J. M. Friesen, P. Glick, M. Fanton, P. Manovi, A. Xydes, T. Bewley, and V. Sunspiral. The second generation prototype of a Duct Climbing Tensegrity robot, DuCTTv2. In *IEEE International Conference on Robotics and Automation*, pages 2123–2128, May 2016.
- [15] M. Furet and P. Wenger. Workspace and cuspidality analysis of a 2-X planar manipulator. In *4th IFToMM Symposium on Mechanism Design for Robotics*, Udine, Italy, September 2018.
- [16] S. Henein. *Conception des structures articulées à guidages flexibles de haute précision*. PhD thesis, École polytechnique fédérale de Lausanne, 2000.
- [17] S. Hirai, Y. Koizumi, M. Shibata, M. Wang, and L. Bin. Active shaping of a tensegrity robot via pre-pressure. In *IEEE/ASME International Conference on Advanced Intelligent Mechatronics*, pages 19–25, July 2013.
- [18] B. de Jager. Design for shape control of tensegrities. In *American Control Conference*, pages 2528–2533, June 2006.

- [19] T. Kaufhold, F. Schale, V. Böhm, and K. Zimmermann. Indoor locomotion experiments of a spherical mobile robot based on a tensegrity structure with curved compressed members. In *IEEE International Conference on Advanced Intelligent Mechatronics*, pages 523–528, July 2017.
- [20] M. Kovac, M. Fuchs, A. Guignard, J. Zufferey, and D. Floreano. A miniature 7g jumping robot. In *2008 IEEE International Conference on Robotics and Automation*, pages 373–378, May 2008.
- [21] D. L Bakker, D. Matsuura, Y. Takeda, and J. Herder. Design of an Environmentally Interactive Continuum Manipulator. In *The 14th IFToMM World Congress*, 2015.
- [22] S. Lessard, D. Castro, W. Asper, S. D. Chopra, L. B. Baltaxe-Admony, M. Teodorescu, V. SunSpiral, and A. Agogino. A bio-inspired tensegrity manipulator with multi-DOF, structurally compliant joints. In *IEEE/RSJ International Conference on Intelligent Robots and Systems*, pages 5515–5520, October 2016.
- [23] F. Li and R. E. Skelton. Sensor/actuator selection for tensegrity structures. In *Proceedings of the 45th IEEE Conference on Decision and Control*, pages 2332–2337, December 2006.
- [24] Q. Li, R. E. Skelton, and J. Yan. Energy optimization of deployable tensegrity structure. In *Proceedings of the 30th Chinese Control Conference*, pages 2146–2151, July 2011.
- [25] K. Liu, J. Wu, G. H. Paulino, and H. J. Qi. Programmable Deployment of Tensegrity Structures by Stimulus-Responsive Polymers. *Scientific Reports*, 7(1):3511, June 2017.
- [26] B. Mehrafrooz, M. Mohammadi, and M. T. Masouleh. Kinematic Sensitivity Evaluation of Revolute and Prismatic 3-DOF Delta Robots. In *5th RSI International Conference on Robotics and Mechatronics*, pages 225–231, October 2017.
- [27] K. W. Moored, T. H. Kemp, N. E. Houle, and H. Bart-Smith. Analytical predictions, optimization, and design of a tensegrity-based artificial pectoral fin. *International Journal of Solids and Structures*, 48(22):3142–3159, November 2011.

- [28] M. Rodelo, J. L. Villa, J. Duque, and E. Yime. Kinematic Analysis and Performance of a Planar 3rrr Parallel Robot with Kinematic Redundancy using Screw Theory. In *IEEE 2nd Colombian Conference on Robotics and Automation*, pages 1–6, November 2018.
- [29] A. P. Sabelhaus, J. Bruce, K. Caluwaerts, P. Manovi, R. F. Firoozi, S. Dobi, A. M. Agogino, and V. SunSpiral. System design and locomotion of SUPERball, an untethered tensegrity robot. In *IEEE International Conference on Robotics and Automation*, pages 2867–2873, May 2015.
- [30] F. A. dos Santos, A. Rodrigues, and A. Micheletti. Design and experimental testing of an adaptive shape-morphing tensegrity structure, with frequency self-tuning capabilities, using shape-memory alloys. *Smart Mater. Struct.*, 24(10):105008, September 2015.
- [31] M. Schenk, S. D. Guest, and J. L. Herder. Zero stiffness tensegrity structures. *Int. J. of Solides and Structures*, 44(20):6569–6583, 2007.
- [32] R. E. Skelton, R. Adhikari, J. P. Pinaud, W. Chan, and J. W. Helton. An introduction to the mechanics of tensegrity structures. In *Proceedings of the 40th IEEE Conference on Decision and Control*, volume 5, pages 4254–4259 vol.5, 2001.
- [33] K. Snelson. Continuous tension, discontinuous compression structures, 1965.
- [34] S. Sumi, V. Böhm, F. Schale, and K. Zimmermann. Compliant Gripper Based on a Multistable Tensegrity Structure. In *New Trends in Mechanism and Machine Science*, Mechanisms and Machine Science, pages 143–151. Springer, Cham, 2017.
- [35] S. Sumi, V. Böhm, and K. Zimmermann. A multistable tensegrity structure with a gripper application. *Mechanism and Machine Theory*, 114:204–217, August 2017.
- [36] A.G. Tibert and S. Pellegrino. Deployable Tensegrity Reflectors for Small satellites. *Journal of Spacecraft and Rockets*, 39(5):702–709, 2002.
- [37] Rafael E. Vasquez, Carl D. Crane, III, and Julio C. Correa. Analysis of a Planar Tensegrity Mechanism for Ocean Wave Energy Harvesting. *Journal of Mechanisms and Robotics*, 6(3):031015–031015–12, June 2014.

- [38] P. Wenger and D. Chablat. Kinetostatic Analysis and Solution Classification of a Planar Tensegrity Mechanism. In Saïd Zeghloul, Lotfi Romdhane, and Med Amine Laribi, editors, *Computational Kinematics*, Mechanisms and Machine Science, pages 422–431. Springer International Publishing, 2018.
- [39] Sebastian Wolf, Giorgio Grioli, Oliver Eiberger, Werner Friedl, Markus Grebenstein, Hannes Höppner, Etienne Burdet, Darwin G. Caldwell, Raffaella Carloni, Manuel G. Catalano, Dirk Lefeber, Stefano Stramigioli, Nikos Tsagarakis, Michaël Van Damme, Ronald Van Ham, Bram Vanderborght, Ludo C. Visser, Antonio Bicchi, and Alin Albu-Schäffer. Variable Stiffness Actuators: Review on Design and Components. *IEEE/ASME Transactions on Mechatronics*, 21(5):2418–2430, October 2016.
- [40] T. Yoshikawa. Manipulability of Robotic Mechanisms. *The International Journal of Robotics Research*, 4(2):3–9, June 1985.